Published in final edited form as:
Magn Reson Imaging. 2011 June ; 29(5): 668–682. doi:10.1016/j.mri.2011.02.012.

Automated Registration of Sequential Breath-Hold Dynamic Contrast-Enhanced MRI Images: a Comparison of 3 Techniques

Sivaramakrishnan Rajaraman[1], **Jeffery J. Rodriguez**[1], **Christian Graff**[2], **Maria I. Altbach**[3], **Tomislav Dragovich**[4], **Claude B. Sirlin**[5], **Ronald L. Korn**[6], and **Natarajan Raghunand**[3,4,*]

[1] Department of Electrical & Computer Engineering, The University of Arizona, Tucson, AZ, USA

[2] Program in Applied Mathematics, The University of Arizona, Tucson, AZ, USA

[3] Department of Radiology, The University of Arizona, Tucson, AZ, USA

[4] Cancer Center, The University of Arizona, Tucson, AZ, USA

[5] Dept. of Radiology, The University of California, San Diego, CA, USA

[6] Scottsdale Medical Imaging Ltd., Scottsdale, AZ, USA

Abstract

Dynamic Contrast-Enhanced MRI (DCE-MRI) is increasingly in use as an investigational biomarker of response in cancer clinical studies. Proper registration of images acquired at different time-points is essential for deriving diagnostic information from quantitative pharmacokinetic analysis of these data. Motion artifacts in the presence of time-varying intensity due to contrast-enhancement make this registration problem challenging. DCE-MRI of chest and abdominal lesions is typically performed during sequential breath-holds, which introduces misregistration due to inconsistent diaphragm positions, and also places constraints on temporal resolution vis-à-vis free-breathing. In this work, we have employed a computer-generated DCE-MRI phantom to compare the performance of two published methods, Progressive Principal Component Registration and Pharmacokinetic Model-Driven Registration, with Sequential Elastic Registration (SER) to register adjacent time-sample images using a published general-purpose elastic registration algorithm. In all 3 methods, a 3-D rigid-body registration scheme with a mutual information similarity measure was used as a pre-processing step. The DCE-MRI phantom images were mathematically deformed to simulate misregistration which was corrected using the 3 schemes. All 3 schemes were comparably successful in registering large regions of interest (ROIs) such as muscle, liver, and spleen. SER was superior in retaining tumor volume and shape, and in registering smaller but important ROIs such as tumor core and tumor rim. The performance of SER on clinical DCE-MRI datasets is also presented.

Keywords

dynamic; gadolinium; MRI; mutual information; non-rigid registration; elastic registration; tracer kinetics

*Correspondence to: Natarajan Raghunand, The University of Arizona, Arizona Cancer Center, 1515 N. Campbell Avenue, Tucson, AZ 85724-5024, U.S.A.; Tel: (520) 626-6041, Fax: (520) 626-6041, raghunan@email.arizona.edu.

INTRODUCTION

DCE-MRI is emerging as a valuable investigational tool for assessing tumor microcirculation in cancer patients treated with anti-angiogenic or anti-vascular agents. In DCE-MRI, images are acquired before, during and after injection of a Gadolinium (Gd)-based MRI contrast agent. MRI contrast agents approved for clinical use are typically small molecules which readily extravasate from tumor microvasculature into the extravascular extracellular space (EES). Pixel-by-pixel pharmacokinetic (PK) analysis of DCE-MRI contrast agent kinetics can be employed to derive physiologically meaningful model parameters which contain quantitative information pertaining to tumor microvascular leakage, vascular volume fraction and perfusion [1,2]. The expectation is that changes in these PK model parameters can serve as imaging biomarkers of tumor response to anti-angiogenic and anti-vascular therapies. Such pixel-by-pixel PK analysis of DCE-MR images is susceptible to misregistration of successive images in the DCE-MRI time-series, as may arise from inconsistent breath-holding, cardiac pulsatility, and gastrointestinal movement. Hence, registration of DCE-MR images is often needed prior to performing any PK analysis. Soft tissues are non-rigid, and rigid registration schemes cannot by themselves provide pixel-by-pixel registration. Fast and efficient non-rigid registration schemes would be of great value in this application.

Image registration algorithms can be classified into two categories, feature-based and intensity-based schemes. Both schemes assume that the anatomical features in the template and source images are the same. However, in DCE-MRI, the spatially-varying kinetics of contrast agent (CA) distribution produces time-varying image contrast, with consequent appearance and disappearance of image features. There is abundant literature on the problem of registration of DCE-MR images, particularly with respect to breast lesions [3,4,5] rather than abdominal lesions. An information-theoretic similarity measure called mutual information has been widely used to register DCE-MR images, since contrast enhancement prohibits direct comparison of the image intensities. Mutual information has also been utilized for aligning images acquired using multiple modalities [6]. Early techniques modeled global motion using affine transformation while the local motion was modeled using free-form deformation based on B-splines [3]. Recently, Wu et al. [7] have employed elastic registration using a normalized cross-correlation similarity metric to register DCE-MR breast images. Hill and co-workers [8] have used iterative dynamic programming, originally devised to solve the stereo matching problem, to register DCE-MR images of the breast. Minardi et al. [9] have proposed a 3-D registration method for DCE-MR images of liver volumes which combines rigid and non-rigid approaches. In this method, a 3-D rigid registration which maximizes normalized mutual information is followed by a 2-D non-rigid registration algorithm based on the complex discrete wavelet transform. All the above-mentioned techniques register post-contrast images to the pre-contrast template. However, as already stated, the features in DCE-MRI images are time-variant. Recently, Li et al. have proposed an adaptive bases algorithm for non-rigid co-registration to a common image space of breast DCE-MRI data sets obtained in separate imaging sessions [10]. Schemes have also been proposed to perform registration based on a PK model [11,12,13]. Xiaohua et al. [11] have developed a scheme for simultaneous segmentation and registration which uses K-means clustering for initial segmentation, followed by fine segmentation based on a PK model. A Markov random field model is incorporated into the framework to reduce the effects of random noise. Buonaccorsi and colleagues have proposed an iterative registration scheme in which the motion-corrupted data is fitted to a PK model to obtain maps of the model parameters [13]. A synthetic data series is generated from these parameter maps by forward solving the PK model. This algorithm identifies the registration parameters by analyzing a small ROI around the tumor using only rigid transformations. These registration parameters are then applied to the whole image, forming a newly registered data series. The

generation of synthetic images using PK model fitting is a time-consuming and complex process. Additionally, the registration may be biased due to incorrect choice of PK model, which would optimize the initial estimates to incorrect values. A novel scheme based on principal components analysis (PCA) has been proposed by Melbourne et al. [14]. A synthetic data series free of motion, but containing the enhancement information, is obtained by reconstructing the data series using only the first few principal components [14]. A fluid registration scheme has also been proposed for registering the synthetic data series with the original data [15]. This scheme, which is referred to as Progressive Principal Component Registration, is applied iteratively. A potential pitfall of this scheme is that the first iteration uses only the first principal component for reconstructing the synthetic data. This may lead to bias in the registration process due to loss of enhancement information contained in the remaining principal components, thereby affecting subsequent iterations.

Intensity variations between adjacent time-sample images in breath-hold DCE-MRI are typically relatively small. A general-purpose non-rigid registration algorithm [16] which explicitly incorporates local changes in brightness and contrast, could thus be expected to perform well at registering such images. We have compared the performances of sequential elastic registration ("Sequential Registration"), a pharmacokinetic model-driven non-rigid registration scheme ("Model-Driven Registration") [13], and the Progressive Principal Component Registration scheme ("Principal Components Registration") [14]. A DCE-MRI computer-generated phantom data series, created by adapting work reported previously [17], is used to compare the performance of the three registration schemes. With all 3 schemes, a 3-D rigid-body registration with mutual information similarity metric was used as a pre-processing step for correcting global registration errors. This step is necessary for reducing computational time and for improving the accuracy of the general-purpose non-rigid registration. The best-performing algorithm, in terms of registration accuracy in the DCE-MRI phantom, was then used to register abdominal and thoracic DCE-MRI data acquired on human subjects in clinical studies.

METHODS

Pharmacokinetic Modeling

Pixel-by-pixel pharmacokinetic analysis of DCE-MRI data was performed using a two-compartment model [1,2]. Three physiologically relevant model parameters were fitted for each pixel, the volume transfer constant (K^{trans}), volume fraction of the extravascular extracellular space (v_e), and plasma volume fraction (v_p). The model can be expressed in the following form:

$$C_t(t)=K^{trans}\int_0^t C_p(\tau)e^{-\frac{K^{trans}(t-\tau)}{v_e}}d\tau+v_pC_p(t) \quad [1]$$

where $C_p(t)$ is the arterial input function (AIF), and $C_t(t)$ is the volume-averaged concentration of the CA in a pixel. $C_t(t)$ was calculated assuming a linear dependence of signal enhancement on the concentration of CA, from the known *in vitro* longitudinal relaxivity of the CA. We employed a bi-exponential population-averaged form of the AIF to estimate $C_p(t)$, as described in equation [2][18]:

$$C_p(t)=D(a_1\exp(-m_1t)+a_2\exp(-m_2t)) \quad [2]$$

Here, D is the dose per kilogram patient weight, m_1 and m_2 are the rate constants (min^{-1}) corresponding to the distribution and clearance phases, respectively, and a_1 and $a_2$are their

amplitudes (kg L^{-1}). The value of D = 0.1 mM kg^{-1}, a_1 = 3.69 kg l^{-1}, a_2 = 4.77 kg l^{-1}, m_1 = 0.144 min^{-1} and m_2 = 0.011 min^{-1} [18]. K^{trans}, v_p and v_e were estimated by multiple linear regression after linearizing Eq. [1] to the form described by Murase [19].

DCE-MRI Registration

We implemented three different schemes for registering DCE-MR images, Sequential Registration, Model-Driven Registration and Principal Components Registration. The performance of Sequential Registration is compared with the latter two schemes. A flow-chart depicting the three schemes is given in Figure 1a.

Global Rigid-Body Registration

This pre-processing step corrects for rigid-body misregistration in all three dimensions, and was applied to all three schemes evaluated in this study. The correction included translation and rotation in the X & Y dimensions and translation in the Z dimension. Two similarity measures were used, normalized and regional mutual information [20,21]. The rationale for including this pre-processing step was two-fold. The first is that the final elastic registration in all three registration schemes is performed between two 2-D images; a simple rigid-body registration performed in the X and Y dimensions reduced the run-time of the more complex elastic registration algorithm. Secondly, while generating the synthetic images using the PK model and PCA, a set of 2-D images at different time points from the same slice is required. The rigid-body registration in the Z dimension ensured that the slices selected for generating the synthetic images closely corresponded to the same physical slice in the Z dimension at all time samples.

Pharmacokinetic Model-Driven Registration

This scheme is a modification of the algorithm proposed by Buonaccorsi et al. [13], wherein the PK model given in Eq. [1] controls the DCE-MR image registration. The modification is that we perform non-rigid registration between the entire synthetic and the original images as opposed to rigid-body registration of just the tumor region in the original work. The synthetic data series were produced as follows. After the initial rigid-body registration (pre-processing) was performed, 2-D images corresponding to a given slice at all the time points were selected. A pixel-by-pixel fit of the 2-D data series to \Eq. [1] yielded parameter maps of K^{trans}, v_p and v_e. With these parameter maps as the starting point, and using the AIF described in Eq. [2], the PK model in Eq. [1] was solved forward to produce a set of synthetic time-series images corresponding to that particular slice. This synthetic data is motion-free, but the PK parameter maps from which they were calculated may have been influenced by motion. At this point, individual 2-D elastic registration [16] was applied between the original and synthetic data series. The entire procedure was repeated for five iterations and the iteration with the lowest model fit mean squared error (MSE) was selected as the registered dataset [13].

Progressive Principal Component Registration

This scheme uses PCA-based synthetic image generation for each slice by the method of Melbourne and co-workers [14]. Briefly, the mean intensity of each time frame was subtracted from every pixel in that frame. Next, a covariance matrix between the images at every time was formed, and from this matrix the eigenvectors were generated. Eigenvectors were then arranged in descending order of their eigenvalues. The arranged eigenvectors form the principal components. The Principal Components Registration scheme is based on the idea that the first few principal components contain signal associated with enhancement, while the remaining principal components contain signal associated with short-term random motion [14]. Accordingly, only the first few principal components are used for

reconstructing the synthetic datasets. Individual 2-D elastic registration [16] was then performed between the original and the synthetic data series. This entire procedure was repeated for *N-1* iterations, *N* being the number of time-samples in the DCE-MRI series. In each iteration, the number of principal components used for reconstructing the synthetic dataset is equal to the iteration number.

Sequential Elastic Registration

In the clinical data employed in this work, breath-hold DCE-MRI was performed on human subjects who were asked to follow a "breathe-in, breathe-out, hold" breathing pattern which typically afforded a temporal resolution of around 16 s per time sample. At this temporal resolution, it was noticed that intensity changes between adjacent time-sample images were small enough as to permit sequential elastic registration. In this scheme, adjacent time-sample images were registered directly using a general purpose elastic registration scheme [16]. For example, the image at the first time-sample (t_0) is used as the template against which the image at the next time-sample (t_1) was registered. The registered t_1 image is then used as the template against which the image at the next time-sample (t_2) is registered, and so on. This process was carried out sequentially through to the final time-sample.

General Purpose Elastic Registration

This step was common to all 3 schemes (Figure 1a). We have employed a general-purpose elastic registration algorithm developed by Periaswamy and Farid [16]. In this algorithm, the geometric transformation is a local affine model with a global smoothness constraint. Intensity variations are explicitly modeled with local changes in brightness and contrast. The estimate of model parameters at every pixel, and the MSE metric applied to the intensity values, corrects the nonlinear distortion. A least-squares technique minimizes the error function which is linear in the model parameters. Then, a nonlinear smoothness constraint is augmented to the linear error function. An iterative nonlinear minimization scheme uses the solution of the least square minimization as the initial estimate to minimize the nonlinear error function. The formulation of the registration algorithm is provided in the Appendix.

Computer-generated Phantom Data

A computer-generated phantom of DCE-MRI images was created by adapting the work reported previously [17]. High-resolution photographic images were obtained from the Visible Human Project [22]. These images were hand-segmented into 14 different tissue types. Mean values of K^{trans}, v_e, v_p, and pre-contrast T1 were assigned to each tissue type based on values reported in the literature as well as from our own measurements (Table 1). These 4 parameters were treated as independent, and their values were distributed randomly among the pixels within a tissue type by assuming a normal distribution with standard deviation of 5% about the mean. This was done in order to mimic the heterogeneity of K^{trans}, v_e, v_p, and pre-contrast T_1 that would normally exist even within a given tissue type. Banerji et al. [23] have also reported the development of a computer-generated phantom for DCE-MRI.

The concentration of CA over time in each pixel was calculated using Eq. [1], the above-generated maps of K^{trans}, v_e, v_p and pre-contrast T_1 (T_{10}), and an AIF modeled using Eq. [2]. The corresponding variation in post-contrast T_1 ($T_1(t)$) over time in each pixel was calculated using Eq. [3]:

$$C_t(t)=\frac{1}{r_1}\left[\frac{1}{T_1(t)}-\frac{1}{T_{10}}\right] \quad [3]$$

where $r_1$wa s assumed to be 4.3 $mM^{-1}s^{-1}$. In turn, the $T_1(t)$ values at every pixel over time were converted to phantom DCE-MRI images using the gradient-echo signal equation:

$$S(t)=S_0\sin(\alpha)\frac{1-\exp(-T_R/T_1(t))}{1-(\cos(\alpha)\exp(-T_R/T_1(t)))} \quad [4]$$

where $S(t)$ is the signal intensity in a given pixel, S_0 is related to the proton density, α is the flip angle, and T_R is the repetition time. For the purposes of these simulations, it was assumed that the echo time TE ≪ T_2.

DCE-MRI phantom images obtained from the high-resolution photographic images were down-sampled to the standard clinical resolution of 256 × 256. This was accomplished by converting the high-resolution phantom DCE-MRI images to k-space values using the 2D Discrete Fourier Transform, followed by sub-sampling in the k-space domain, and conversion back to 256 × 256 time-series images by means of 2D Inverse Discrete Fourier Transform. A second phantom DCE-MRI dataset with noise was created analogously, by introducing independent zero-mean Gaussian noise to both the real and imaginary components of k-space prior to sub-sampling in k-space. Since the phantom has 10 times the resolution of the MR images, it adequately approximates a continuous object, including in-plane partial volume effects. In order to incorporate through-slice partial volume effects at clinical imaging resolutions, a 3-D tumor ROI was placed randomly along the slice direction. Since the DCE-MRI phantom images were created from known "ground truth" K^{trans}, v_e and v_p maps, they were used to test the performance of the 3 registration schemes.

Clinical DCE-MRI Protocol

DCE-MRI was performed in accordance with local IRB regulations, and informed consent was obtained from human subjects with advanced solid tumors who were recruited into ongoing Phase 1 clinical studies of two investigational anti-cancer drugs. Imaging was performed on either 1.5 T or 3 T MRI scanners. DCE-MRI data were collected by imaging subjects who repeated a "breathe-in, breathe-out, hold" pattern, with the imaging occurring during each held-expiration period. DCE-MRI data used in this work are from 4 subjects, 2 of whom were imaged once at baseline and once post-treatment, and 2 who were imaged once at baseline and twice post-treatment. For the purposes of this work, baseline and post-treatment scans could be treated as independent, for a total of 10 registration experiments. 16 distinct tumors were chosen for registration, including 1 lung, 1 chest wall, 1 uterine and 13 liver lesions. Primary tumor histologies included leiomyosarcoma, NSCLC, pancreatic, and colorectal cancers.

Prior to the dynamic portion of the scanning, 4 pre-contrast 3D-GRE images were obtained at flip angles of 15°, 23°, 30° and 60° so that a pre-contrast T_{10} map could be calculated in each case. The dynamic series portion of the imaging comprised of 24–30 3D-GRE images collected during repeated "held exhalation" breath-holds. This afforded a temporal resolution of 16–18 seconds in the DCE-MRI series. Typical parameters for the 3D-GRE imaging were, 12 slices reconstructed to a matrix size of 256 × 256, slice thickness = 5 mm, T_R = 5.0 ms, T_E = 2.1 ms, and α=30°. After 1–2 pre-contrast images had been acquired, gadolinium contrast was injected at a dose of 0.1 mmole/kg at a rate of 4 mL/s using a power-injector, and chased with a 20 mL saline flush also injected at 4 mL/s.

Quantitative Assessment of Registration Accuracy

We generated a phantom dataset with 5 slices and 30 time points to compare the performance of the three registration algorithms in terms of registration accuracy. Relative

to the assumed field-of-view of 34 cm, a 13 mm × 6.5 mm ellipsoidal tumor was introduced in the middle 3 of 5 slices. A survey of the literature did not reveal previously published models for defining the motion and deformation observed in sequential breath-hold DCE-MRI data. Consequently we assessed 3 deformation schemes, including deformation using a polynomial function, affine deformation in the X and Y directions followed by deformation using a polynomial function, and random movement of rows and columns in either direction by one pixel. By visual assessment on a trial-and-error basis, we found deformation by polynomial functions to be most representative of the misregistration that was evident in our clinical DCE-MRI datasets. Motion corruption was introduced in the DCE-MRI phantom by deforming the images in the 3 tumor-containing slices using a forward and reverse polynomial function to define the spatial relation of the pixels between the actual and the deformed image. The forward function used in our simulation is given by:

$$y(:,:)=x(:,:)^{\wedge}n \qquad [5]$$

where *y(:,:)* is the position of a pixel in the deformed image, *x(:,:)* is the position of the same pixel in the actual image and *n* is the degree of the polynomial function. The transformation defined by the above function was applied on the actual images and bilinear interpolation was used to generate the deformed images. The degree of the polynomial function determined the amount of deformation introduced in the image. For a given slice, the images at different time-samples were deformed using different degrees between 0.95 and 1.05 generated by a pseudo-random number algorithm. Post-deformation, the images were visually observed to make sure that the motion deformations were substantial but within the range observed in clinical data. This noise-free “motion-corrupted” phantom dataset was registered using the 3 registration schemes.

The above-mentioned steps were also repeated with a second phantom dataset which incorporated noise (SNR of 50 dB), to test the robustness of the registration schemes. The addition of noise led to degradation in the pixel-by-pixel PK model fit, and a change in the ground truth PK parameter values relative to the noise-free phantom dataset.

The framework for quantitatively and qualitatively assessing registration accuracy is presented in Figure 1b. The first metric was a comparison of the mean PK parameter values for different ROIs, before and after registration, with the known ground truth parameter values. For each registration scheme, mean ROI parameter values post-registration were compared with the ground truth PK parameter values to ascertain the performance of the registration algorithm. The other two metrics for assessing registration accuracy were the *MSE* between the actual and the fitted concentration of CA over time, and the multiple linear correlation coefficient (*CC*) values obtained from the PK model fitting, as defined in Eq. [6] and [8], respectively.

$$MSE=\frac{\sum_{i=1}^{N}(Y_i - Y_{FIT})^2}{N-p-1} \qquad [6]$$

$$MST = \frac{\sum_{i=1}^{N} (Y_i - \overline{Y})^2}{N - 1} \quad [7]$$

$$CC = 1 - \frac{MSE}{MST} \quad [8]$$

Here N is the number of time-samples used for the PK model fitting, Y_i is the concentration of the CA over time for the pixel under test, Y_{FIT} is the fitted concentration of the CA over time for the pixel under test, Y is the average concentration of CA for the pixel under test, *MST* is mean square total, p is number of coefficients used in the PK model fitting. From Eq. [6] for *MSE*, we infer that as the images get registered, the actual pixel intensity values over time will better correspond to the PK model, thereby reducing the *MSE* metric. In the case of *CC*, as the images get registered, the coefficient values will approach the value of 1, indicating a better correspondence between the PK model and actual pixel intensity values over time.

RESULTS

Comparison of the Registration Schemes by PK Values

The DCE-MRI phantom was constructed to depict the abdominal region since the majority of our clinical data were acquired on human subjects with hepatic lesions. Figure 2 shows the results for the 3 registration schemes in phantom datasets with and without noise. ROIs were hand-drawn around muscle, liver, spleen and tumor. In addition, ROIs were drawn around the tumor rim (comprising a strip approximately 2 pixels wide inside the tumor perimeter), tumor core (the rest of the tumor), and muscle rim (comprising a strip approximately 3 to 4 pixels wide along the edge of the muscle). Addition of nonlinear deformations to the phantom caused significant changes in the PK parameter estimates relative to the ground truth. In particular, large deviations were noticed in the tumor core, tumor rim and muscle rim, all of which are comprised of relatively few pixels (about 20 pixels for the tumor rim ROI, 40 pixels for the tumor core, and 40 pixels for the muscle rim). By comparison, PK parameters in larger ROIs (about 200 pixels) corresponding to muscle, spleen and liver were less susceptible to change upon deformation. This was to be expected, since the ROIs selected for muscle, spleen and liver were relatively far from the edges of the respective organs, such that deformation was less likely to produce “mixing” with a different tissue.

The average deviations in the PK parameter values in tumor core and tumor rim were as large as 196% relative to the ground truth values. All three registration schemes satisfactorily restored the PK values (average deviation of 5.7 % from the ground truth) in larger ROIs like muscle, spleen and liver; in figure 2 results are shown only for muscle, but results in liver and spleen followed the same pattern. In the case of tumor core and tumor rim, the Sequential Registration scheme was able to restore the values closer to the ground truth (average deviation of 14.7 ± 7.7 % from the ground truth) when compared to Principal Components Registration (average deviation of 39.5 ± 24.67 % from the ground truth) and Model-Driven Registration (average deviation of 39.2 ± 15.85 % from the ground truth). For muscle rim, the average deviation pre-registration was 43.07 ± 17.07 % from the ground truth. Sequential Registration was able to restore the PK values closer to ground truth (average deviation of 4.23 ± 2.11 % from the ground truth) when compared to Principal

Components Registration (average deviation of 33.65 ± 30.45 % from the ground truth) and Model-Driven Registration (average deviation of 17.82 ± 16.32 % from the ground truth).

Comparison of the Registration Schemes by MSE

All 3 registration schemes showed an improvement in the *MSE* post-registration against the pre-registration values (Table 2). A reduction in *MSE* indicates improved correspondence of pixel-by-pixel intensity values over time to the PK model. For the phantom dataset without noise, the *MSE* values for tumor rim and tumor core showed a greater reduction from the pre-registered values in the case of Sequential Registration when compared to the other two schemes. The *MSE* values for muscle showed a greater reduction from the pre-registered values in the case of Principal Components Registration when compared to the other two schemes. However, in the case of the phantom data with noise, Principal Components Registration returned the lowest *MSE* values in all the three ROIs. The phantom dataset contains salt and pepper noise in the DCE-MRI images which is smoothed by the general-purpose registration algorithm. This algorithm is utilized once per iteration of the three different registration schemes. Both Principal Components Registration and Model-Driven Registration are iterative schemes, and with increase in number of iterations, the smoothing effect in the images increases. Of the 3 registration schemes, Principal Components Registration had the highest number of iterations for registration, and the salt and pepper noise was virtually eliminated and led to the lowest *MSE*. This is followed by Model-Driven Registration, with 5 iterations. The single-iteration Sequential Registration scheme returned the highest *MSE* among the 3 schemes. For the ground truth phantom dataset without noise, the calculated *MSE* was not exactly equal to zero. This stems from the manner of generation of the software phantom, wherein K^{trans}, v_e and v_p were treated as spatially independent even within a tissue type, and their values distributed randomly among the pixels within a tissue type by assuming a normal distribution with standard deviation of 5% about the mean. This meant that, even in the absence of noise, there was a small but non-zero *MSE*.

Qualitative Comparison of the Registration Schemes

Figure3 depicts a qualitative comparison of the performance of the 3 registration schemes. All the three registration techniques led to a significant correction of the nonlinear distortion introduced in the DCE-MRI phantom. It was observed that the shape of the tumor was distorted following Model-Driven Registration and Principal Components Registration, leading to appearance of misregistered edges in the difference images (Figures 3g-h), while the shape of the tumor was better preserved in the case of Sequential Registration (Figure 3i). It should be noted that this distortion artifact in the tumor introduced by Model-Driven Registration and Principal Components Registration was not reflected in the corresponding *MSE* values listed in table 2. This was because the observed distortion in the shape of the tumor was relatively uniform across all the time-samples in the DCE-MRI series, including the first time-sample image on which ROIs were drawn around tumor core and tumor rim. Volume and shape distortions have been noted previously in other non-rigid techniques for registering DCE-MR images [4, 5]. Rohlfing et al. report that intensity-based registration algorithms are particularly prone to producing size distortions – in their experience, reductions in breast lesion size by up to 78% after registration – and have proposed a novel incompressibility constraint to reduce such distortions [4].

In order to quantify the distortion in tumor shape post-registration, a subsection (about 20 × 20 pixels) of the image around the tumor was extracted from the ground truth dataset as well as the data sets after Sequential Registration, Principal Components Registration and Model-Driven Registration. The mutual information between each of these 3 post-registration image subsections and the corresponding subsection from the ground truth dataset were calculated. The mutual information values over all time-points for the three registration

schemes are depicted in Figure 4a. Registration using Sequential Registration produced the highest mutual information value, reflecting better preservation of tumor shape, relative to Principal Components Registration and Model-Driven Registration. The relatively low mutual information after Principal Components Registration reflects the increase in size of the tumor following registration that is visible in Figures 3e and 3h. A plot of the variation of signal intensity over time in the whole tumor ROI from the undistorted, pre-registration and post-registration phantom datasets is shown in Figure 4b. Agreement of the undistorted phantom data with data registered using Sequential Registration was generally better than with data registered using Model-Driven Registration and Principal Components Registration.

When compared to Principal Components Registration and Model-Driven Registration, for tumor core and tumor rim, Sequential Registration 1) restored the PK parameter values closer to the ground truth, 2) had the lowest *MSE* values in the dataset without noise, 3) preserved the shape of the tumor post-registration, and 4) better matched signal intensity over time in the tumor ROI relative to the ground truth dataset. For these reasons, Sequential Elastic Registration was selected as the preferred algorithm for registration of clinical DCE-MRI datasets.

Sequential Elastic Registration of Clinical DCE-MRI Data

Since the ground truth PK parameter values are not known for the clinical DCE-MRI data from human subjects, we have used qualitative analysis and the *MSE* metric to evaluate the performance of Sequential Registration in reducing motion errors. We obtained a quantitative evaluation of Sequential Registration from the difference images given in Figure 5. Figure 5a shows the anatomical image pre-registration and Figure 5b, c and d shows the anatomical image post-registration for the initial, middle and the late enhancement stage in the DCE-MRI series. Figure 5e, f, g and h shows the corresponding difference images with the image at the previous time-sample in the same DCE series. Comparing Figure 5e with Figure 5f, g and h, we can observe that motion errors are reduced at the boundaries of the spleen, tumor, liver, aorta and the skin. The poor registration in the top right-hand corner of the image (Figure 5g) is due to the presence of gastrointestinal motion which could not be adequately registered using Sequential Registration.

The reduction in motion errors post-registration can also be seen in plots of the concentration of the CA over time for different tumor ROIs pre- and post-registration (figures 6a–b). We can observe that the concentration curve for the CA over time becomes smoother post-registration in all 3 ROIs, which is indicative of a reduction in misregistration following Sequential Registration. A smoother concentration curve post-registration leads to improvement in PK model fitting, which was further captured by reduction in the *MSE* metric post-registration.

The results for the *MSE* for all the 10 clinical datasets (1a–b, 2a–b, 3a–c, 4a–c) are provided in Figure 7. The *MSE* for the unregistered (original) data is taken to be 100, and the corresponding percentage change in *MSE* for the dataset after Sequential Registration is depicted. A reduction in the *MSE* metric was observed in 56 out of 63 ROIs analyzed over the 10 datasets after Sequential Registration. The results for all the patient datasets except for 2a, 2b showed considerable reduction in the *MSE* metric. The tumor ROI in dataset 2a, 2b was very close to the heart, and the resulting blurring of the image degraded the performance of the general-purpose elastic registration algorithm.

The numerical values for *MSE* and corresponding change in the PK parameter values following Sequential Registration are provided in Tables 3a–c for 3 lesions in a particular patient who was imaged on 3 visits. Sequential Registration produced a significant reduction

in *MSE*, which was indicative of improved registration between successive time samples. There was also a considerable change in the values of the PK parameters post-registration, which would impact the diagnostic utility of these data. For example, on the baseline scans of this patient (table 3a), in tumor no. 1 Sequential Registration produced a 17.5% reduction in mean K^{trans}, a 27.4% reduction in mean v_e, and a 5.8% increase in mean v_p. In tumor no. 2, Sequential Registration produced a 46.7% reduction in mean K^{trans}, a 39.8% reduction in mean v_e, and a 45% reduction in mean v_p. In tumor no. 3, Sequential Registration produced an 8.5% increase in mean K^{trans}, a 27% increase in mean v_e, and a 8.9% reduction in mean v_p in the baseline scan for patient 3

DISCUSSION AND CONCLUSIONS

The simulations were carried out on a 1392-core SGI Altix ICE 8200 high-performance computing cluster, with each node being a 2.83 GHz quad-core Xeon processor with 2GB memory per core. The general-purpose elastic registration was the most time-consuming step in all 3 schemes. For Principal Components Registration and Model-Driven Registration, the original data series were registered with synthetic data series, thereby making each individual 2-D registration independent of others. This property could be exploited to run the individual iterations in parallel. Individual 2-D registrations in Sequential Registration are dependent on the previous time-sample, and this method is not parallelizable. However this was compensated by the fact that Sequential Registration is a single iteration scheme. On our system it took approximately 5 minutes to register a given source image to a given target image. Thus, in a scenario where the number of available processors was not limiting, for a DCE-MRI dataset with *N*time -samples, Principal Components Registration took (*N*-1)*5 “wall clock” minutes, Model-Driven Registration took approximately 5*5 “wall clock” minutes (for 5 iterations), and Sequential Registration took *N*5 “wall clock” minutes. For situations in which the number of available computing nodes is limiting, a comparison of the 3 schemes on the basis of total “CPU minutes” required to register all the time-samples in a single slice is more useful. In the terms of “CPU minutes”, Principal Components Registration took *N*-1 times as long to run, and Model-Driven Registration took approximately 5 times as long to run, when compared to the run-time of Sequential Registration.

We have developed a computer-generated DCE-MRI phantom to compare the performance of Sequential Registration with Principal Components Registration and Model-Driven Registration. While individualized AIFs are desirable for accurate measurements of pharmacokinetic parameters from clinical DCE-MRI data, we have utilized a population AIF in our DCE-MRI phantom. Our rationale is that the best algorithms for registering entire DCE-MRI images may not necessarily also be the best for registering only arterial pixels. More restricted and computationally less-demanding algorithms may perform better in registering only arterial pixels. We have therefore utilized a population AIF, to eliminate the AIF as a factor that would confound a comparison of the 3 algorithms tested in this work. There was a superior overall performance of Sequential Registration over the other two schemes in simulations carried out on the DCE-MRI phantom data series. In small ROIs such as tumor core and tumor rim, Sequential Registration restored the PK parameter values closer to the ground truth, had the lowest *MSE* values in the dataset without noise, preserved better the post-registration shape of the tumor, and better matched signal intensity over time in the tumor ROI relative to the ground truth dataset, when compared to Principal Components Registration and Model-Driven Registration.

Registration experiments were also carried out on 10 different DCE-MRI datasets obtained from human subjects with abdominal and thoracic lesions. Due to the absence of ground truth in these clinical datasets, the performance of Sequential Registration was analyzed

using qualitative difference images, and by a comparison of the pre- and post-registration *MSE* metric calculated between the actual and fitted concentration of CA over time. Sequential Registration showed a reduction in the *MSE* metric in 56 out of the total 63 ROIs analyzed in the clinical datasets post-registration. The reduction in the *MSE* metric indicates that post-registration, concentration values of a voxel over time matches better with the PK model. In these registration experiments, the subject was assumed to be immobile during the 10 second acquisition of each image. Motion is to be expected even during breath-hold; cardiac and peristaltic motion effects will always be present, and the subject may unintentionally move. However, it is reasonable to assume that any motion during the breath-hold would be small in comparison to the misregistration occurring during the free-breathing period between image acquisitions. We have therefore focused this work on compensating for the misregistration between image acquisitions. Motion that occurs during image acquisition is a secondary effect which would warrant a separate investigation.

Sequential Elastic Registration, being a serial registration scheme, is susceptible to the propagation of registration errors across time-samples. For example, Skrinjar et al. report that in a cardiac cine MRI application, reference-based registration was more accurate than sequential registration [24]. Nonetheless, we have investigated the utility of sequential registration on the rationale that changes in image intensity between successive time-samples in breath-hold DCE-MRI are small enough for a general-purpose registration scheme to be effective. In situations where the assumption of small changes between sequential images does not hold, the sequential elastic registration method would be prone to an accumulation of errors and other methods may become more suitable. As these results indicate, sequential elastic registration is a viable option for registering breath-hold DCE-MR images, potentially improving the diagnostic value of pharmacokinetic model analysis of such data.

Acknowledgments

This work was partly funded by grants from the National Institutes of Health (P01-CA017094 and the IRAT supplement to P30-CA023074).

References

1. Kety SS. The theory and applications of the exchange of inert gas at the lungs and tissues. Pharmacol Rev. 1951; 3:1–41. [PubMed: 14833874]
2. Tofts PS. Modeling tracer kinetics in dynamic Gd-DTPA MR imaging. J Magn Reson Imaging. 1997; 7:91–101. [PubMed: 9039598]
3. Rueckert D, Sonoda LI, Hayes D, Hill DLG, Leach MO, Hawkes DJ. Nonrigid registration using free-form deformations: Application to breast MR images. IEEE Trans Med Imaging. 1999; 18:712–721. [PubMed: 10534053]
4. Rohlfing T, Maurer CR, Bluemke DA, Jacobs MA. Volume-preserving non-rigid registration of MR breast images using free-form deformation with an incompressibility constraint. IEEE Trans Med Imaging. 2003; 22:730–741. [PubMed: 12872948]
5. Tanner, C.; Schnabel, JA.; Chung, D.; Clarkson, MJ.; Rueckert, D.; Hill, DLG.; Hawkes, DJ. Volume and shape preservation of enhancing lesions when applying nonrigid registration to a time-seriesof contra st enhancing MR breast images. Proceedings of the 3rd International Conference on MICCAI; Pittsburgh, PA, USA. 2000. p. 327-337.
6. West JB, Fitzpatrick JM, Wang MY, Dawant BM, Maurer CR Jr, Kessler RM Jr, Maciunas RJ, Barillot C, Lemoine D, Collignon A, Maes F, Suetens P, Vandermeulen D, Van den Elsen PA, Napel S, Sumanaweera TS, Harkness B, Hemler PF, Hill DLG, Hawkes DJ, Studholme C, Maintz JBA, Viergever MA, Malandain G, Pennec X, Noz ME, Maguire GQ, Pollack M Jr, Pelizzari CA, Robb RA, Hanson D, Woods RP. Comparison and evaluation of retrospective intermodality image registration techniques. J Comput Assisted Tomogr. 1997; 21:554–566.

7. Wu, Q.; Whitman, GJ.; Fussell, DS.; Markey, MK. Registration of DCE-MR images for computer-aided diagnosis of breast cancer. Proceedings of the 40th ACSSC; Monterey, California, USA. 2006. p. 826-830.
8. Hill, A.; Mehnert, A.; Crozier, S.; Leung, C.; Wilson, S.; McMahon, K.; Kennedy, D. Dynamic breast MRI: Image registration and its impact on enhancement curve estimation. Proceedings of the 28th IEEE EMBS Annual International conference; New York City, NY, USA. 2006. p. 3049-3052.
9. Minardi LT, Passera KM, Lucesoli A, Potepan P, Setti E, Musumeci R. A method for dynamic subtraction MR imaging of the liver. BMC Med Imaging. 2006; 6:5. [PubMed: 16759378]
10. Li X, Dawant BM, Welch EB, Chakravarthy AB, Freehardt D, Mayer I, Kelley M, Meszoely I, Gore JC, Yankeelov TE. A nonrigid registration algorithm for longitudinal breast MR images and the analysis of breast tumor response. Magn Reson Imaging. 2009; 27:1258–1270. [PubMed: 19525078]
11. Xiaohua, C.; Brady, M.; Lo, JLC.; Moore, N. Simultaneous segmentation and registration of contrast-enhanced breast MRI. Proceedings of the 19th International Conference on IPMI; USA: Glenwood Springs, CO; 2005. p. 126-137.
12. Hayton P, Brady M, Tarassenko L, Moore N. Analysis of dynamic MR breast images using a model of contrast enhancement. Med Image Anal. 1997; 1:207–224. [PubMed: 9873907]
13. Buonaccorsi GA, O'Connor JPB, Caunce A, Roberts C, Cheung S, Watson Y, Davies K, Hope L, Jackson A, Jayson GC, Parker GJM. Tracer kinetic model-driven registration for dynamic contrast-enhanced MRI time-series data. Magn Reson Med. 2007; 58:1010–1019. [PubMed: 17969122]
14. Melbourne A, Atkinson A, White MJ, Collins D, Leach M, Hawkes D. Registration of dynamic contrast-enhanced MRI using a progressive principal component registration (PPCR). Phys Med Biol. 2007; 52:5147–5156. [PubMed: 17762077]
15. Crum WR, Tanner C, Hawkes DJ. Anisotropic multi-scale fluid registration: evaluation in magnetic resonance breast imaging. Phys Med Biol. 2005; 50:5153–5174. [PubMed: 16237247]
16. Periaswamy S, Farid H. Elastic registration in the presence of intensity variations. IEEE Trans Med Imaging. 2003; 22:865–874. [PubMed: 12906240]
17. Graff, C.; Clarkson, E.; Outwater, E.; Altbach, M. Computer-generated abdominal phantom for evaluation of MR estimation techniques. Proceedings of the 16th Annual Meeting of the ISMRM; Toronto, Canada. 2008. (Abstract 492)
18. Ahearn TS, Staff RT, Redpath TW, Semple SIK. The effects of renal variation upon measurements of perfusion and leakage volume in breast tumors. Phys Med Biol. 2004; 49:2041–2051. [PubMed: 15214540]
19. Murase K. Efficient method for calculating kinetic parameters using T1-weighted dynamic contrast-enhanced magnetic resonance imaging. Magn Reson Med. 2004; 51:858–862. [PubMed: 15065262]
20. Studholme C, Hill DLG, Hawkes DJ. An overlap invariant entropy measure of 3-D medical image alignment. Pattern Recog. 1999; 32:71–86.
21. Russakoff, DB.; Tomasi, C.; Rohlfing, T.; Maurer, C. Image similarity using mutual information of regions. Proceedings of the 8th ECCV, Prague, Czech Republic; 2004. p. 596-607.
22. Ackerman MJ. Visible human project. Proceedings of the IEEE. 1998; 86:504–511.
23. Banerji, A.; Caunce, A.; Watson, Y.; Rose, C.; Buonaccorsi, G.; Parker, G. A flexible software phantom for generating realistic dynamic contrast-enhanced MR images of abdominal tumors. Proceedings of the 16th Annual Meeting of the ISMRM; Toronto, Canada. 2008. (Abstract 493)
24. Skrinjar O, Bistoquet A, Tagare H. Symmetric and transitive registration of image sequences. Int J Biomed Imaging. 200810.1155/2008/686875
25. Barron JL, Fleet DJ, Beauchemin SS. Performance of optical flow techniques. International J Comput Vision. 1994; 12:43–77.
26. Heeger DJ. Optical flow using spatio-temporal filters. International J Comput Vision. 1988; 1:279, 302.
27. Lucas, BD.; Kanade, T. An iterative image registration technique with an application to stereo vision. Proceedings of the 7th IJCAI; Vancouver, Canada. 1981. p. 679

Appendix

As explained elsewhere [16], the general purpose elastic registration algorithm borrows its formulation from the field of motion estimation [25,26,27]. $f(\hat{x}, \hat{y}, t)$ and $f(\hat{x}, \hat{y}, t-1)$ denotes the source and target images respectively. Initially, the geometric transformation contains a local affine model and then, a global nonlinear smoothness constraint is imposed. The initial affine model with an explicit change of local contrast and brightness is given by:

$$m_7 f(x, y, t) + m_8 = f(m_1\hat{x} + m_2\hat{y} + m_5, m_3\hat{x} + m_4\hat{y} + m_6, t-1) \quad [1]$$

Here, m_1, m_2, m_3, m_4 are the linear affine parameters, m_5, m_6 are the translation parameters and m_7, m_8 are parameters related to contrast and brightness, respectively. The error function uses the MSE metric. A first-order Taylor series expansion approximates the error function, after which the error function is of the form:

$$E_b(\vec{m}) = \sum_{x,y\in\Omega} [k - \vec{c}^{\mathrm{T}}\vec{m}]^2 \quad [2]$$

where:

$$k = f_t + x f_x + y f_y \quad [3]$$

$$\vec{c} = (\ x f_x \quad y f_x \quad x f_y \quad y f_y \quad f_x \quad f_y \quad -f \quad -1\ )^T \quad [4]$$

Differentiating the error function with respect to the unknowns, setting the result equal to zero and solving, we obtain:

$$\frac{dE_b(\vec{m})}{d\vec{m}} = \sum_{x,y\in\Omega} -2\vec{c}[k - \vec{c}^{\mathrm{T}}\vec{m}] \quad [5]$$

Now, the linear error function is augmented with a nonlinear smoothness constraint:

$$\vec{m} = \left[\sum_{x,y\in\Omega} \vec{c}\,\vec{c}^{\,T}\right]^{-1} \left[\sum_{x,y\in\Omega} \vec{c}\,k\right] \quad [6]$$

Here, $(\vec{m})$ is given by Eq. [2] and $(\vec{m})$ is given by the following equation:

$$E(\vec{m}) = E_b(\vec{m}) + E_s(\vec{m}). \quad [7]$$

where λ_i is a positive constant that controls the relative weight given to the smoothness constraint on parameter m_i. Differentiating with respect to the model parameters, setting it to zero and solving for $\vec{m}$ minimizes the new error function. The equation becomes highly intractable to solve analytically and hence, an iterative scheme is used to solve for $\vec{m}$ given by:

$$E_s(\vec{m}) = \sum_{i=1}^{8} \lambda_i \left[\left(\frac{\partial m_i}{\partial x} \right)^2 + \left(\frac{\partial m_i}{\partial y} \right)^2 \right] \quad [8]$$

where

$$\vec{m}^{(j+1)} = (\vec{c}\,\vec{c}^{\,T} + L)^{-1} (\vec{c}\,k + L\bar{\vec{m}}^{j}) \quad [9]$$

is a component-wise average of $\vec{m}$ over a small spatial neighborhood and L is an 8 × 8 diagonal matrix with diagonal elements λ_i. Eq. [6] gives the initial estimate for $\vec{m}^{(0)}$.

A differential multiscale framework corrects for large- and small-scale deformations. In the multiscale framework, a Gaussian pyramid with T levels is built for both template and source images with level 0 being the coarse image and level T being the smoothest. The local affine, contrast and brightness parameters are estimated at level 0. These parameters warp the source image in the next level of the Gaussian pyramid. A new estimate of the parameters is computed at the next level. The above-mentioned process repeats through each level of the pyramid. The transformations at each level of the pyramid accumulate yielding a single set of final transformation parameters.

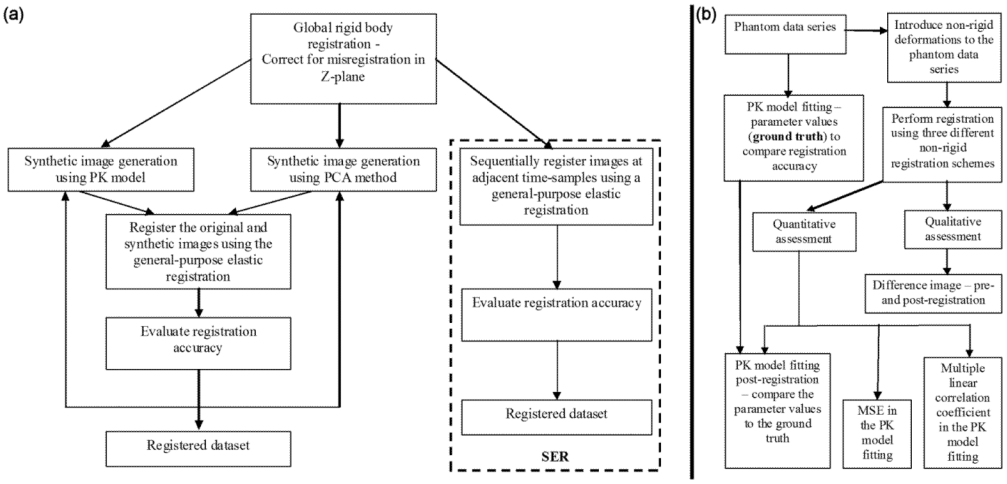

Figure 1.

(a) Sequential Elastic Registration (SER), Progressive Principal Component Registration (PPCR) and Pharmacokinetic Model-Driven Registration (PMDR) registration schemes; (b) Scheme for measurement of registration accuracy.

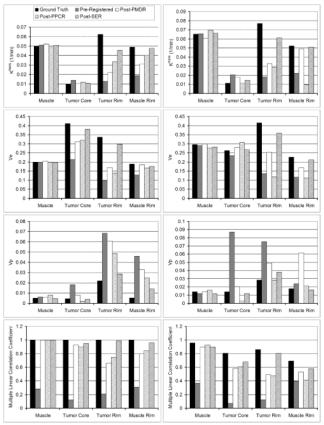

Figure 2.

Mean values of K^{trans}, v_e, v_p, and correlation coefficients from the PK model fit in the computer-generated phantom, after nonlinear motion corruption and after registration by Sequential Elastic Registration (SER), Pharmacokinetic Model-Driven Registration (PMDR) and Progressive Principal Component Registration (PPCR), compared against the ground truth parameter values. Left column = results from phantom data without noise, Right column = phantom data with added noise.

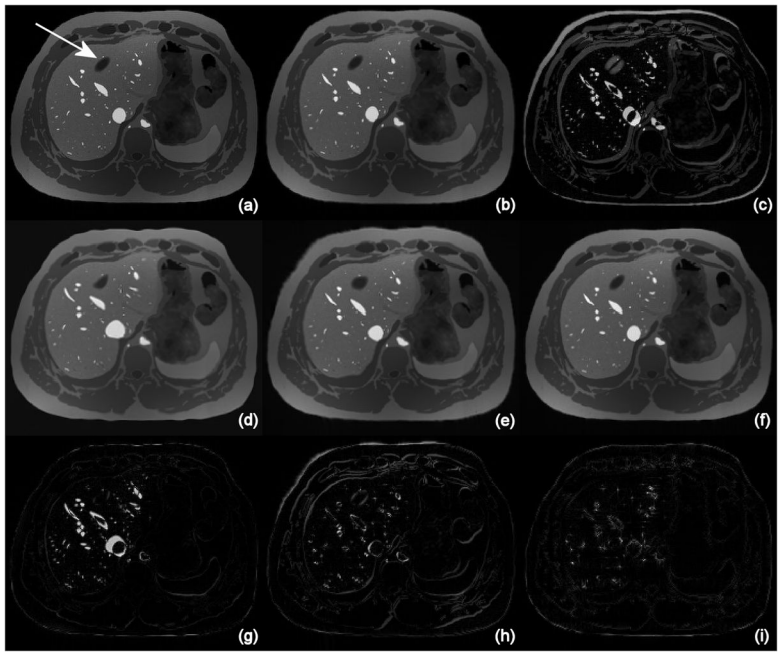

Figure 3.

Results from the 3 different registration schemes, on an example slice and time-point in the software DCE-MRI phantom: **(a)** Ground truth phantom slice (arrow indicates tumor). **(b)** Phantom slice after nonlinear deformation. **(c)** Difference image between **a** and **b**, showing the extent of the deformation. **(d)** Phantom slice after registration using Pharmacokinetic Model-Driven Registration. **(e)** Phantom slice after registration using Progressive Principal Component Registration. **(f)** Phantom slice after registration using Sequential Elastic Registration. **(g–i)** Absolute difference images between **d-f**, respectively, and **a.** The difference images **c**, **g**, **h** and **i** are scaled between 0–255 using a common scaling factor for display purpose.

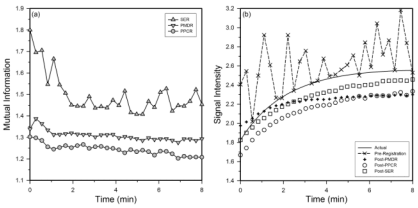

Figure 4.

Comparison of Sequential Elastic Registration (SER), Pharmacokinetic Model-Driven Registration (PMDR) and Progressive Principal Component Registration (PPCR) based on (**a**) degree of preservation of tumor shape (**b**) Signal intensity vs. time for the whole tumor ROI in the DCE-MRI phantom.

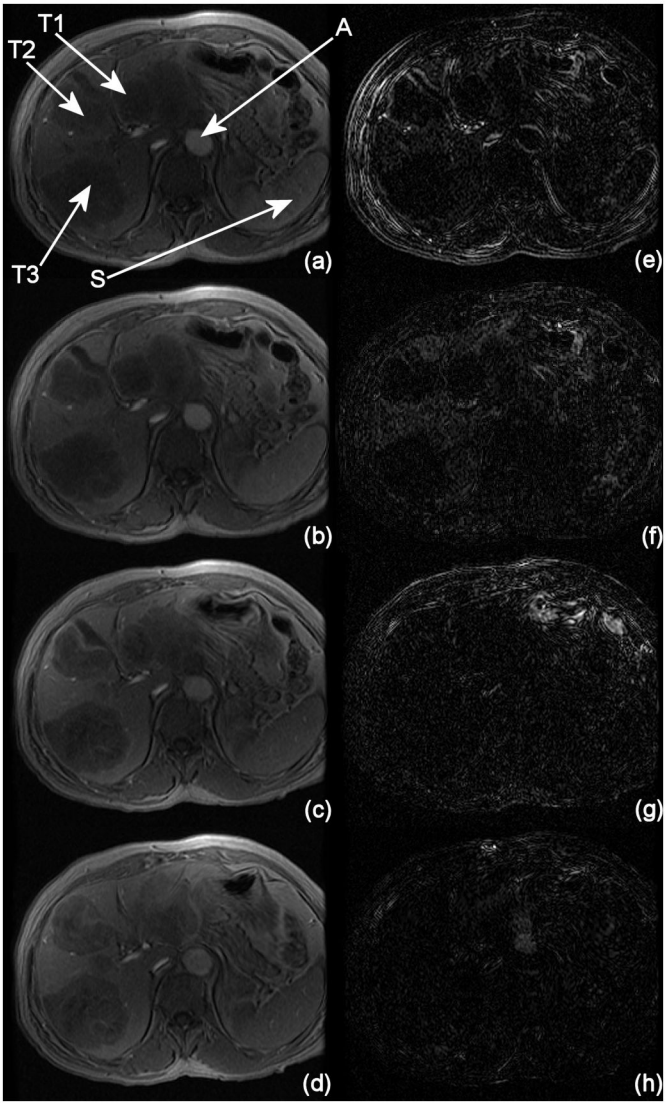

Figure 5.

Absolute difference images demonstrating successful registration with Sequential Elastic Registration. (**a**) unregistered post-contrast image (T1, T2, T3 – tumors, A – Aorta, S – Spleen). (**b**), (**c**) and (**d**) are registered post-contrast image at the initial, middle and late enhancement stage respectively. (**e**), (**f**), (**g**) and (**h**) are the corresponding difference image with the previous time-sample image in the DCE-MRI series. All the difference images are displayed with equal scaling for intensity.

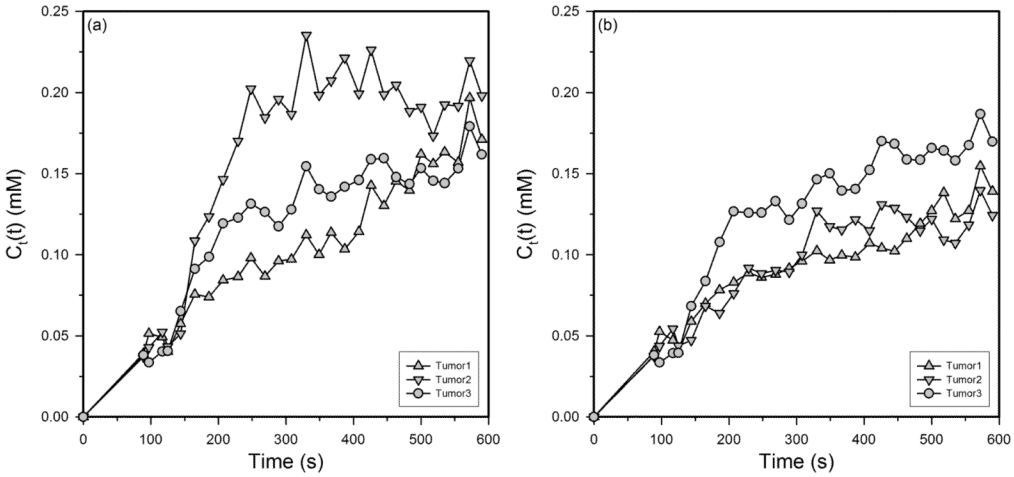

Figure 6.

Comparison of the concentration of CA over time (**a**) pre-registration, and (**b**) after Sequential Elastic Registration, for three tumors from patient dataset 3a.

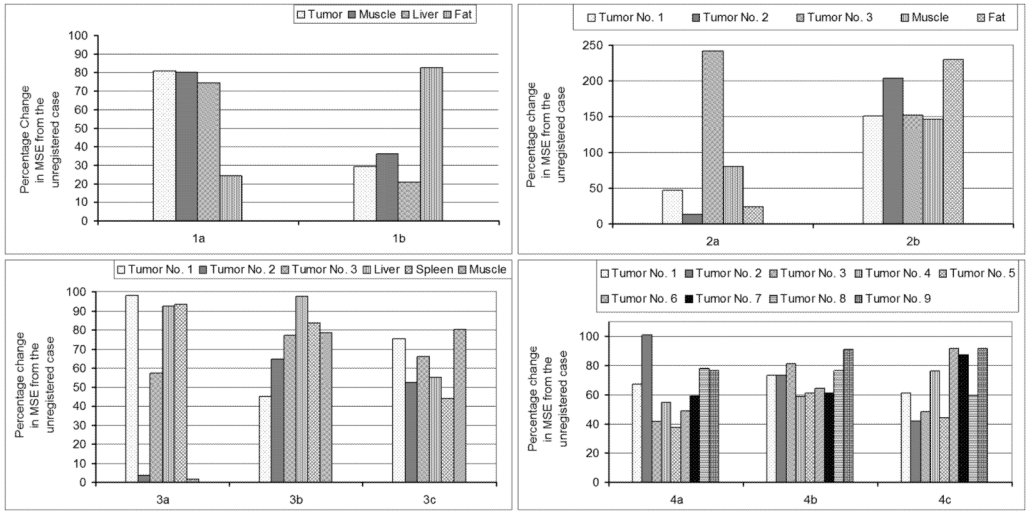

Figure 7.

MSE between actual and fitted concentration of the CA to the PK model. Result shows the values relative to the 100% pre-registration values for all the clinical datasets registered using Sequential Elastic Registration. Each bar-chart gives the results obtained from the baseline and post-treatment scans of one patient.

Table 1

Mean values of K^{trans}, v_e and v_p used for different tissue types in the phantom dataset.

Tissue Type	K^{trans} (min^{-1})	v_e (dimensionless)	v_p (dimensionless)	T_1 (ms)
Spleen	0.6	0.3	0.3	1057
Fat	0.03	0.05	0.005	343
Muscle	0.05	0.2	0.005	1130
Stomach	0.05	0.2	0.005	1600
Renal Cortex	0.6	0.1	0.3	1412
Renal Medulla	0.5	0.3	0.1	1412
Gall Bladder	0.09	0.6	0.05	1600
Pancreas	0.09	0.1	0.05	584
Liver	0.09	0.1	0.05	586
Tumor Rim	0.15	0.3	0.04	586
Tumor Core	0.01	0.4	0.0005	1600
Bone	0.001	0.0005	0.0005	549
Cartilage	0.001	0.001	0.0005	1060
Lung	0.02	0.483	0.1218	1000

Table 2

MSE Values for Actual, Pre- and Post- Registration for Phantom Data without and with Noise. PPCR – Progressive Principal Component Registration; PMDR – Pharmacokinetic Model-Driven Registration; SER – Sequential Elastic Registration.

ROI	Phantom without Noise			Phantom with Noise		
	Muscle	Tumor Core	Tumor Rim	Muscle	Tumor Core	Tumor Rim
Actual	8.85E-11	3.77E-07	9.27E-08	6.62E-04	6.25E-04	4.31E-04
Pre-Registration	1.76E-05	1.36E-02	3.46E-03	3.63E-04	6.00E-02	1.14E-02
Post-PPCR	1.16E-06	5.54E-05	3.54E-05	1.74E-04	1.83E-04	2.17E-04
Post-PMDR	1.46E-06	9.11E-06	4.28E-05	2.61E-04	3.25E-04	3.35E-04
Post-SER	2.02E-06	8.29E-06	1.68E-05	2.61E-04	3.32E-04	4.07E-04

Table 3

Pre- and Post- Sequential Elastic Registration Mean PK Parameter Values and *MSE* for the (a) Baseline Scan of Patient 3, (b) First Post-Treatment Scan of Patient 3, (c) Second Post-Treatment Scan of Patient 3.

	Tumor No. 1		Tumor No. 2		Tumor No. 3	
	Pre	**Post**	**Pre**	**Post**	**Pre**	**Post**
MSE	6.83E-03	6.69E-03	3.30E-02	1.17E-03	3.51E-03	2.01E-03
K^{trans} (min^{-1})	4.61E-02	3.80E-02	7.36E-02	3.93E-02	4.24E-02	4.60E-02
v_e	2.85E-01	2.07E-01	3.09E-01	1.86E-01	2.55E-01	3.24E-01
v_p	7.10E-02	7.52E-02	1.34E-01	7.39E-02	1.04E-01	9.45E-02

a

	Tumor No. 1		Tumor No. 2		Tumor No. 3	
	Pre	**Post**	**Pre**	**Post**	**Pre**	**Post**
MSE	3.66E-03	1.64E-03	2.60E-03	1.68E-03	2.10E-03	1.62E-03
K^{trans} (min^{-1})	3.30E-02	3.48E-02	3.64E-02	3.10E-02	3.84E-02	3.86E-02
v_e	2.41E-01	2.10E-01	2.91E-01	2.21E-01	2.58E-01	2.55E-01
v_p	6.29E-02	6.79E-02	6.81E-02	7.06E-02	6.17E-02	5.93E-02

b

	Tumor No. 1		Tumor No. 2		Tumor No. 3	
	Pre	**Post**	**Pre**	**Post**	**Pre**	**Post**
MSE	5.18E-03	3.90E-03	3.19E-03	1.67E-03	3.52E-03	2.32E-03
K^{trans} (min^{-1})	5.40E-02	6.16E-02	4.38E-02	3.37E-02	5.05E-02	5.30E-02
v_e	2.92E-01	2.84E-01	2.30E-01	2.56E-01	2.76E-01	2.50E-01
v_p	9.12E-02	1.04E-01	1.03E-01	1.07E-01	8.43E-02	8.65E-02

c